OES | Opto-Electronic Science

Femtosecond laser rapid customization of high-performance anti-reflection windows

Yulong Ding†, Xiang Jiang†, Cong Wang*, Xianshi Jia*, Linpeng Liu, Weina Han, Zheng Gao, Shiyu Wang, Nai Lin, Dejin Yan and Ji'an Duan

https://doi.org/10.29026/oes.2026.260004

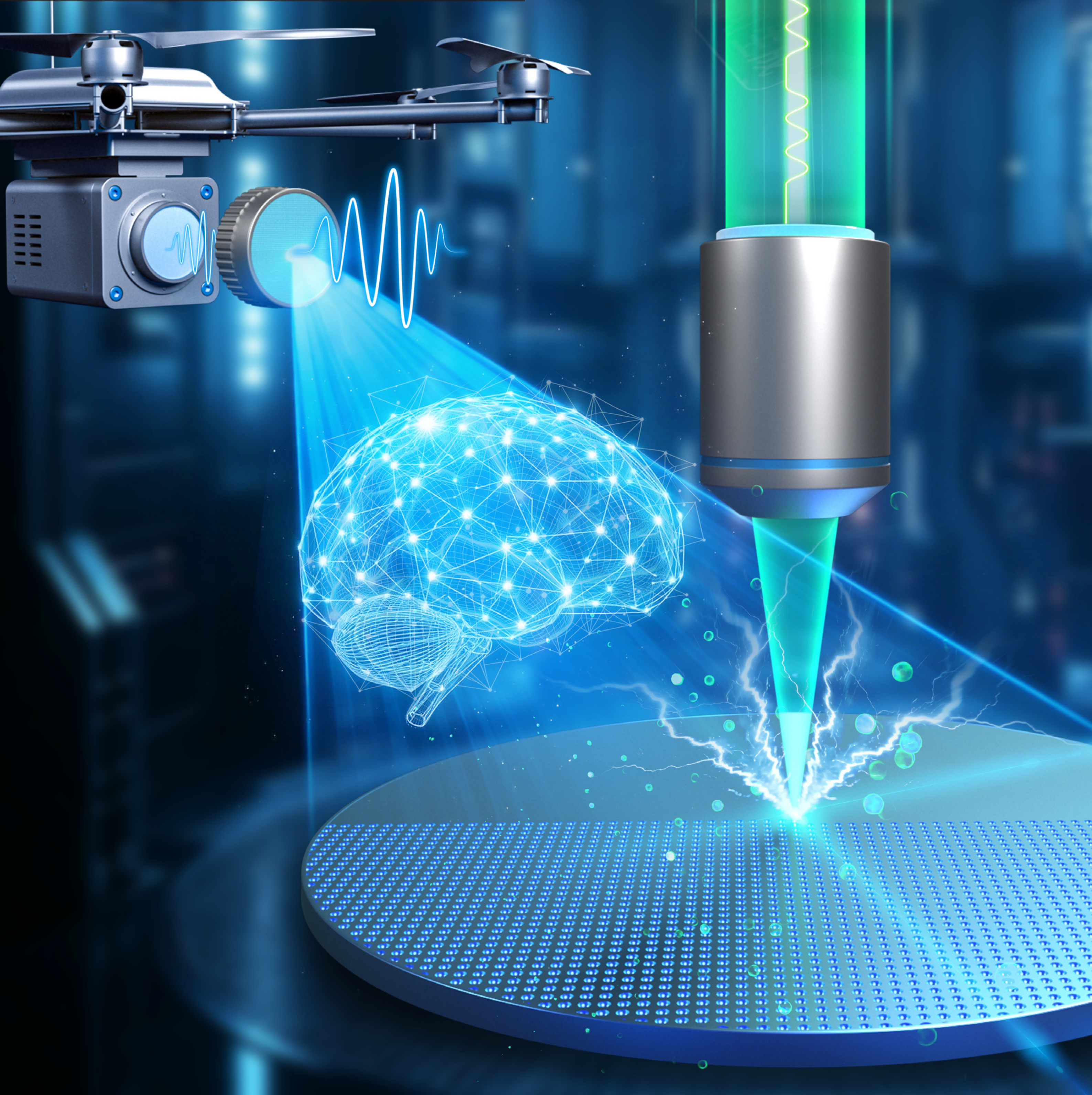

Opto-Electronic Science

CN 51-1800/O4 ISSN (Print) 2097-0382 ISSN (Online) 2097-4000

Femtosecond laser rapid customization of high-performance anti-reflection windows

Yulong Ding, Xiang Jiang, Cong Wang*, Xianshi Jia*, Linpeng Liu, Weina Han, Zheng Gao, Shiyu Wang, Nai Lin, Dejin Yan and Ji'an Duan

Citation: Ding YL, Jiang X, Wang C et al. Femtosecond laser rapid customization of high-performance anti-reflection windows. *Opto-Electron Sci* **5**, 260004 (2026).

https://doi.org/10.29026/oes.2026.260004

Received: 27 January 2026; Accepted: 20 March 2026; Published online: 23 April 2026

Related articles

Femtosecond laser micro/nano-processing via multiple pulses incubation

Jingbo Yin, Zhenyuan Lin, Lingfei Ji et al

Opto-Electronic Technology 2025, **1**(2): 250003 doi: 10.29026/oet.2025.250003

Dynamic spatial beam shaping for ultrafast laser processing: a review

Cyril Mauclair, Bahia Najih, Vincent Comte et al

Opto-Electronic Science 2025, **4**(8): 250002 doi: 10.29026/oes.2025.250002

CW laser damage of ceramics induced by air filament

Chuan Guo, Kai Li, Zelin Liu et al

Opto-Electronic Advances 2025, **8**(7): 240296 doi: 10.29026/oea.2025.240296

High performance micromachining of sapphire by laser induced plasma assisted ablation (LIPAA) using GHz burst mode femtosecond pulses

Kotaro Obata, Shota Kawabata, Yasutaka Hanada et al

Opto-Electronic Science 2024, **3**(6): 230053 doi: 10.29026/oes.2024.230053

More related articles in Opto-Electronic Journals Group website

OES Opto-Electronic Science

Article

April 2026, Vol. 5, No. 4

Open Access

Femtosecond laser rapid customization of high-performance anti-reflection windows

Yulong Ding[1†], Xiang Jiang[1†], Cong Wang[1*], Xianshi Jia[1*], Linpeng Liu[1], Weina Han[2], Zheng Gao[1], Shiyu Wang[1], Nai Lin[3], Dejin Yan[3] and Ji'an Duan[1]

Abstract: Bionic anti-reflection windows are critical for enhancing the performance of aerospace infrared detection systems. The manufacturing of anti-reflective microstructures (ARMs), however, faces a significant challenge that the transmittance spectrum is difficult to predict both accurately and swiftly, leading to long-term reliance on blind and inefficient trial-and-error for process optimization. Here, we report a method that integrates machine learning (ML) with femtosecond laser for the rapid customization of high-performance anti-reflection windows. Embedding of the material's absorption characteristics as a physical constraint into the ML model enables highly accurate prediction across an ultra-broad transmittance spectrum, overcoming the failure of conventional simulations in these intrinsic absorption bands. The trained ML model serves as an intelligent agent to guide the precise control over multiple femtosecond laser parameters, thus converting the costly process of physical trial-and-error into one of efficient virtual screening and iteration. As a proof of concept, an anti-reflective sapphire window was produced that demonstrates broadband (3.3–6.0 μm) and high transmittance (~96.8% peak at 4.2 μm), along with excellent wide-angle characteristics, mechanical wear resistance, and high-quality imaging capability. This work provides a novel paradigm for rapidly manufacturing high-performance anti-reflective windows, laying the foundation for next-generation optical components.

Keywords: femtosecond laser; machine learning; anti-reflection windows; spectra prediction; infrared detection

DOI: 10.29026/oes.2026.260004 | CSTR: 32246.14.oes.2026.260004

Citation: Ding YL, Jiang X, Wang C et al. Femtosecond laser rapid customization of high-performance anti-reflection windows. *Opto-Electron Sci* **5**, 260004 (2026).

1 Introduction

Nature-inspired micro/nanostructured surfaces, engineered by mimicking biological hierarchical designs, can exhibit extraordinary multifunctional properties[1−3]. These include anti-reflectivity[4], high transmittance[5], controllable wettability[6], and abilities to prevent ice formation or fogging[7]. Such surfaces have garnered significant interest in both civilian and military applications. The pursuit of higher-efficiency signal transmission and superior imaging quality in optical and optoelectronic systems drives the need to minimize reflection losses caused by abrupt refractive index changes at material interfaces[8]. Critical components like optical windows in infrared cameras, solar cells, aircraft, and military hardware face demanding operational conditions. They must endure rapid temperature fluctuations, impacts from sand and dust, mechanical abrasion, and erosion by rain[9]. Conventional anti-reflection coatings (ARCs), widely used in commercial products, often suffer from limitations[4]. Their performance can degrade due to thermal expansion mismatches with the substrate or straightforward wear and tear[10]. To enhance the reliability and longevity of these components in harsh environments, research has increasingly turned to bio-inspired anti-reflective microstructures (ARMs)[11−16]. For example, the compound eyes and wings of the dragonfly are classic and representative bioinspiration

Received: 27 January 2026

Accepted: 20 March 2026

Published online: 23 April 2026

[1]State Key Laboratory of Precision Manufacturing for Extreme Service Performance, College of Mechanical and Electrical Engineering, Central South University, Changsha 410083, China; [2]Laser Micro/Nano Fabrication Laboratory, School of Mechanical Engineering, Beijing Institute of Technology, Beijing 100081, China; [3]The 10th Research Institute of CETC, Chengdu 610036, China.

[†]These authors contributed equally to this work.

*Correspondence: C Wang, E-mail: wangcong@csu.edu.cn; XS Jia, E-mail: 221026@csu.edu.cn

models for anti-reflective optical microstructures, and its gradient refractive index anti-reflection mechanism has been widely recognized and applied in the design and fabrication of bionic anti-reflective optical components (Fig. 1(a)). Many researchers have constructed a gradual refractive index transition layer from air to the window material by fabricating convex or concave subwavelength microstructure arrays on both the upper and lower surfaces of optical windows, effectively reducing reflection loss (Fig. 1(b))[4,9,10,17]. Research demonstrates that ARMs can achieve enhanced optical transmittance over broad bandwidths and wide angles of incidence[9,18]. Beyond their optical function, they simultaneously offer high wear resistance[19], laser damage resistance[14], and anti-contamination properties[5]. This combination of properties makes them promising for reliable service in extreme and complex environments, particularly for infrared detection systems.

The optical performance, particularly the transmittance within specific bands, can be significantly enhanced by optimizing the structural parameters of these microstructures, such as size, period, and morphology[9,20]. Achieving ideal anti-reflective properties, however, demands extremely precise control over these parameters, especially when the required feature sizes approach 1 μm. Advances in micro- and nanofabrication have facilitated the practical application of ARMs. Techniques like electron-beam lithography

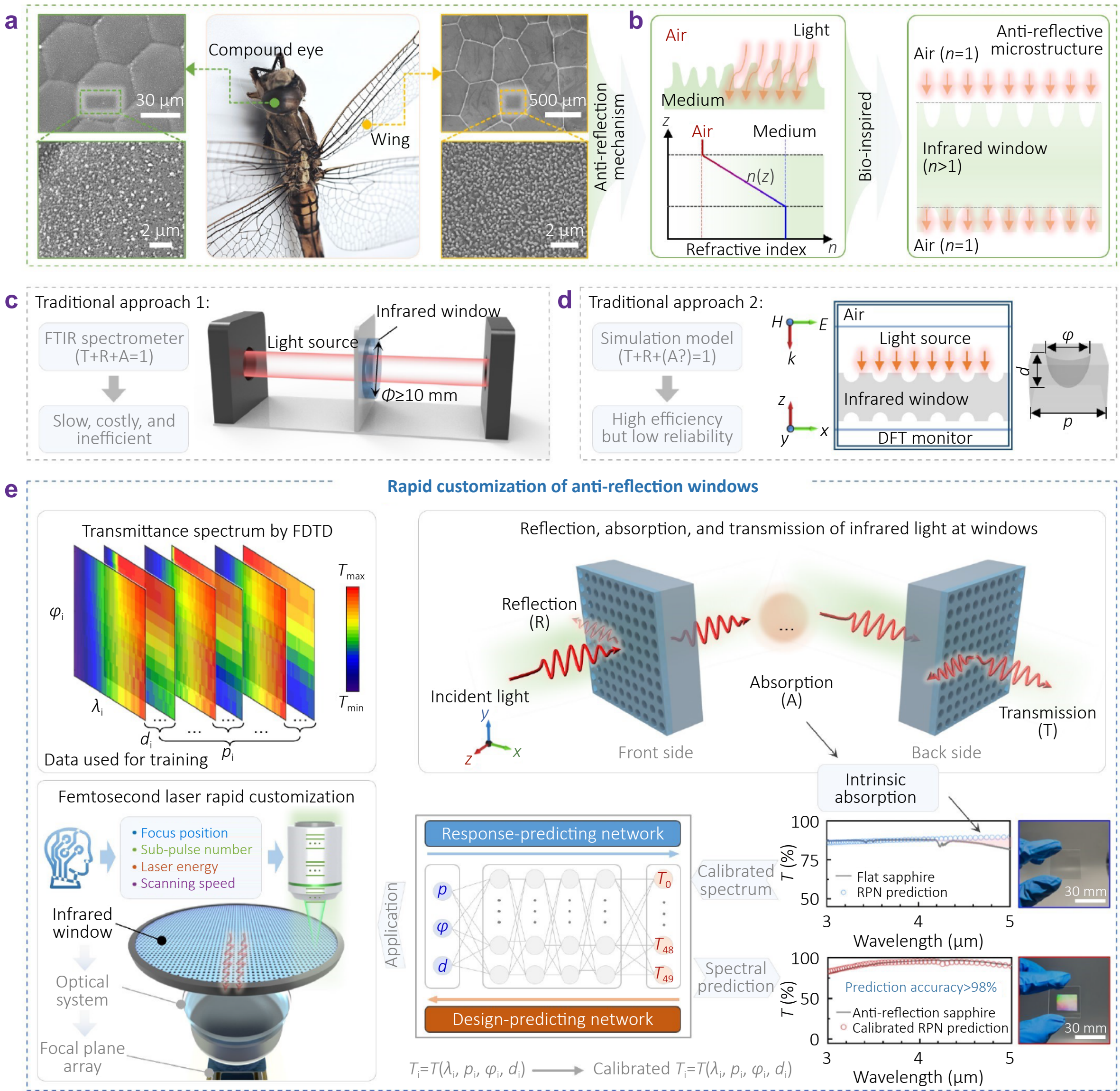

Fig. 1 | Workflow for ML-assisted femtosecond laser fabrication of ARMs. (a) Macroscopic and microscopic images of the compound eyes and wings of the dragonfly. (b) Bio-inspired subwavelength microholes on surfaces and their anti-reflective principles. (c, d) Schematic diagram of the test method and simulation method for obtaining infrared spectra. (e) Schematic diagram of the infrared spectral prediction method developed in this work and its application in laser process optimization.

and nanoimprint lithography enable their high-precision manufacture[21–23]. These methods, nevertheless, often involve high costs and complex procedures. More importantly, they generally lack broad adaptability. Adjusting the manufacturing process to create different microstructures on various window materials or for different application requirements presents a significant difficulty. In recent years, bionic femtosecond laser micro/nano fabrication has emerged as a powerful and versatile strategy for preparing functional optical structures, and it has been widely exploited for the fabrication of light-harvesting, infrared camouflage, information encryption, and optical imaging components for various optical applications[24–26]. Leveraging this bioinspired fabrication strategy, femtosecond laser processing technology has been extensively used for fabricating ARMs on a variety of optical window materials, including diamond[13,27], sapphire[16,28], zinc sulfide[29,30], magnesium fluoride[20,31], and lithium niobate[14]. Its advantages include maskless operation, single-step fabrication, and tunable dimensional parameters[32–39]. Despite these prominent benefits, fabricating broadband, high-transmittance anti-reflective metasurfaces with femtosecond lasers still remains a substantial challenge for practical infrared optical applications. Early research in this field employed point-by-point sculpting to achieve precise microstructure geometry. This approach, however, suffers from extremely low manufacturing efficiency, making it unsuitable for industrial production of metasurfaces that can comprise millions to hundreds of millions of unit cells. For practical fabrication, high-repetition-rate pulse outputs combined with high-speed motion platforms are typically used[40–43]. A single pulse or burst can create over 10,000 anti-reflective micro-units per second[5,44,45]. The structural parameters of microstructures made this way are influenced by multiple laser processing parameters, including laser energy, number of sub-pulses, focusing position, and scanning speed[46–48]. This multi-parameter dependence makes precise control over the final microstructure and the reliable fabrication of ideal structural parameters inherently difficult.

Optimizing the fabrication process is essential for manufacturing optical windows with higher transmittance[4,49]. In theory, identifying suitable processing parameters might require testing hundreds of different laser parameter sets by fabricating and characterizing corresponding samples. Meeting the measurement requirements of a Fourier-transform infrared (FTIR) spectrometer (which typically has a sampling aperture of around 10 mm, as shown in Fig. 1(c)) would mean producing hundreds of large-area samples. This approach consumes substantial human and material resources. Vector diffraction theory provides a rigorous electromagnetic framework for obtaining exact solutions to Maxwell's equations under various boundary conditions[50], making it broadly applicable to arbitrary micro- and nanostructures. Numerical simulation models, such as the finite-difference time-domain (FDTD) method and rigorous coupled-wave analysis[5,11,51,52], are built upon this foundation to predict the transmittance spectra from single ARM. These simulation models, however, face significant challenges in prediction accuracy. A primary limitation is the difficulty in precisely predicting absorption within spectral bands where the window material exhibits intrinsic absorption (Fig. 1(d)). For instance, sapphire, magnesium fluoride, and zinc sulfide all show a marked decrease in transmittance at wavelengths beyond approximately 4.0 μm[16], 5.5 μm[31], and 10.0 μm[5], respectively, due to a significant rise in absorption. These bands are often critical for infrared detection. Published simulation results currently report notable deviations (ranging from 5% to 30%) in transmittance predictions at these wavelengths (Table S1 in Supplementary information). Consequently, simulation models are primarily used to analyze the general influence trends of structural parameter variations on transmittance spectra, rather than for customized, precise spectral prediction[53,54]. Furthermore, designing ARMs using simulation-based approaches often requires extensive prior knowledge and iterative modeling to navigate the complex design space, making efficient optimization challenging. In contrast, machine learning (ML) models trained on simulation data enable millisecond-scale real-time predictions once deployed, offering a dramatic acceleration over conventional simulations. For instance, recent advances demonstrate that neural network-assisted end-to-end designs can efficiently model complex meta-optics for full light field control across multiple wavelengths and polarizations, achieving high-performance multi-color holography and imaging[55,56]. However, the performance of ML methods heavily depends on the quality and coverage of training data, and in the absence of physical constraints, they may generate unphysical predictions. To address these limitations, physics-informed ML, which integrates physical laws with data-driven approaches, has emerged as a promising paradigm for tackling multiphysics and multiscale problems[57–62]. Regarding low-fidelity models, researchers have indicated that a multi-fidelity strategy should first employ a simplified physical solver to generate a large number of approximate samples, followed by model correction using a small amount of high-fidelity observational data, thereby balancing computational efficiency with prediction accuracy[58]. Therefore, constructing a highly reliable ML model for transmittance spectrum prediction, capable of integrating physical constraints and experimental calibration, represents a key enabler for the rapid and customized femtosecond laser fabrication of high-performance anti-reflective windows.

Here, to achieve the rapid and reliable manufacturing of high-performance anti-reflective windows, this work proposes an ML-assisted femtosecond laser processing method. This method constructs a neural network incorporating a spectral calibration layer, enabling high-accuracy prediction (error < 2%) of the transmittance spectra for ARMs for the first time, even within the material's absorption bands. Furthermore, by embedding the trained model as an intelligent agent into the process development cycle, rapid mapping (< 0.1 s) from laser parameters to final optical performance and virtual optimization are achieved. This fundamentally transforms the traditional trial-and-error based paradigm for process development. The fabricated anti-reflective sapphire window serves as a proof of concept, demonstrating broadband performance (3.3–6.0 μm) with a peak transmittance of ~96.8% at 4.2 μm, complemented by excellent wide-angle response, mechanical durability, and high-fidelity imaging. This work thereby establishes a novel paradigm for the rapid customization of high-performance anti-reflective windows, paving the way for next-generation optical components.

2 Results and discussion

2.1 Construction of transmittance spectrum prediction model

Optical windows are critical components in infrared imaging systems, tasked with protecting internal components while ensuring high-quality transmission and reception of infrared signals[63–66]. When infrared light interacts with a window material, it is primarily divided into transmitted, reflected, and absorbed components[51,67]. To achieve high-fidelity imaging, optimizing the parameters of ARMs to minimize reflective losses is essential. The fabrication of these microstructures using a femtosecond laser, however, introduces complexity. Key laser processing parameters, including laser energy, sub-pulse number, focusing position, and scanning speed, collectively influence the final structural geometry. Achieving rapid optimization of these parameters requires real-time feedback on the optical outcome of the machining process. To address this, we propose a machine-learning-assisted framework for fabricating high-performance anti-reflective windows with a femtosecond laser (Fig. 1(e)). The core of this framework is the construction of an efficient and accurate model for predicting transmittance spectra. It is important to note that this methodological framework is applicable to manufacturing high-performance ARMs on the surface of various optical window materials. For the purpose of this demonstration, we employ a sapphire window, a material commonly used in the mid-wave infrared (MWIR, 3–5 μm) band[68,69]. Within this spectral range, sapphire has a refractive index ranging from 1.62 to 1.71, leading to a Fresnel reflection loss of approximately 6% per air-material interface. Optimizing the parameters of the femtosecond laser-fabricated microstructures is therefore necessary to achieve high transmittance (Fig. S1, Supplementary information).

To train the prediction model, a large dataset was generated using the commercial software Ansys Lumerical FDTD Solutions through simulations of three-dimensional hole-type structures. To ensure the simulated structures are both physically meaningful and cover the feasible fabrication space, the parameter ranges were constrained. The ranges for the structural parameters were determined based on diffraction equations, effective medium theory, and classical thin-film theory (Note S1, Supplementary information)[70,71]. The upper and lower bounds of the design space are 1.6 μm ≤ p ≤ 2.0 μm, 0 μm ≤ φ ≤ 2.0 μm, and 0 μm ≤ d ≤ 1.4 μm for data generation (Fig. S2, Supporting Information). We compute the discretized transmittance spectrum $T = [T_0, T_1, T_2, T_3, ..., T_{49}]$ for the design space $[p, \varphi, d]$ in the wavelength range 3 μm ≤ λ ≤ 5 μm . The dataset comprises 16,350 samples, with each sample containing the structural parameters of the holes and the corresponding transmittance at specific wavelengths. The dataset was randomly divided into training, validation, and test sets with a ratio of 70%:15%:15%. A fixed random seed (2025) was used to ensure the reproducibility of the data split and the comparability of different model architectures during subsequent optimization. A bidirectional neural network framework based on multilayer perceptrons was then constructed to achieve rapid mapping between the structure and its optical performance. This framework consists of a Response Prediction Network (RPN) responsible for forward prediction and a Design Prediction Network (DPN) dedicated to inverse design. Considering the intrinsic absorption of sapphire within the 4–5 μm band, an effect that cannot be precisely solved through simulation alone, leading to significant prediction errors in the transmittance spectrum, a calibration layer was incorporated into the output layer of the model. This calibration was performed using data obtained from FTIR spectrometer measurements of a flat sapphire window[72]. The underlying rationale is that while the ARMs primarily alter the transmission efficiency at the interface, the beam's propagation angle within the bulk material remains largely unchanged, thereby keeping the effective optical path length constant (Fig. S3, Supplementary information). The experimental results demonstrate that the calibrated model can be generalized for predicting the transmittance spectra of anti-reflective windows, achieving an accuracy greater than 98%.

The transmittance spectrum prediction model was constructed, trained, calibrated, and applied using the commercial software MATLAB. The bidirectional neural network demonstrated excellent performance in both forward and inverse prediction tasks. In forward modeling, the RPN served as an efficient surrogate for traditional numerical simulations, capable of predicting the transmittance spectrum for any given set of microstructure parameters within milliseconds (Fig. 2(a)). The network was optimized using a mean squared error (MSE) loss function. As shown in Fig. 2(b), the training and validation loss curves converged synchronously and maintained a minimal gap, indicating stable convergence without overfitting and excellent generalization capability throughout the training epochs. Quantitative evaluation further confirmed the RPN's

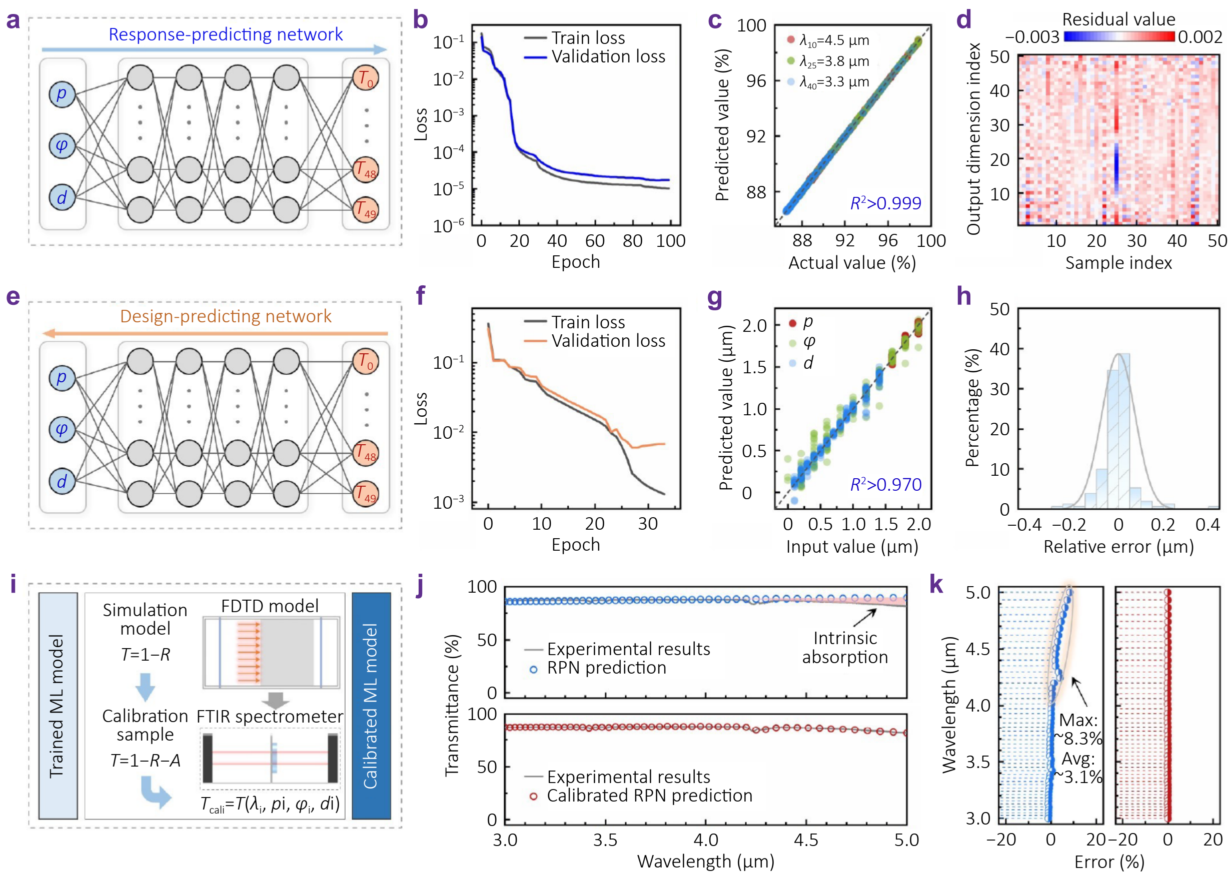

Fig. 2 | Training and calibration of the ML model. (a) Schematic diagram of the framework for the RPN. (b) Training and validation loss curves for the RPN. (c) Regression scatter plot of predicted values versus actual values on the RPN test set (examples include wavelength values of 3.3 μm, 3.8 μm, and 4.5 μm). (d) Distribution of prediction residuals on the RPN test set. (e) Schematic diagram of the framework for the DPN. (f) Training and validation loss curves for the DPN. (g) Regression scatter plot of predicted values versus actual values on the DPN test set. (h) Distribution of prediction errors on the DPN test set. (i) Physical calibration of the trained model. (j, k) Comparison of RPN-predicted transmittance values for sapphire windows and their errors before and after calibration.

reliability. On an independent test set, the model's predictions achieved a coefficient of determination (R^2) greater than 0.999. Regression analysis showed that the predicted and true values were highly concentrated on both sides of the fit line, with absolute residuals predominantly below 0.003 (Fig. 2(c, d)). Furthermore, feeding eight specific structural parameter sets into the trained RPN yielded predicted spectra in close agreement with FDTD simulation results, confirming the high accuracy of this surrogate model (Fig. S4, Supplementary information). For the inverse design task, an early-stopping strategy was employed for the DPN to prevent overfitting and secure optimal generalization performance. The model parameters from the 27th training epoch, corresponding to the lowest validation loss, were selected (Fig. 2(e, f)). The DPN achieved R^2 values above 0.97 for its predictions of the three key structural parameters: period, diameter, and depth. The absolute errors of these predictions were largely confined within 0.1 μm (Fig. 2(g, h)). To validate the DPN's overall efficacy, the microstructure parameters it generated through inverse design were fed back into the RPN for forward verification. The results showed that the transmittance spectra predicted from the DPN-designed parameters closely matched the original target spectra (Fig. S5, Supplementary information). These results demonstrate that the constructed bidirectional neural network framework enables fast and reliable mapping between structural parameters and transmittance spectra. Subsequently, a spectral calibration layer was added to the trained model (Fig. 2(i)). The physical basis for this calibration approach is grounded in the principle of energy conservation, which governs the distribution of incident light into transmitted, reflected, and absorbed components. Conventional simulation methods such as FDTD typically assume that the material exhibits no intrinsic absorption, leading to an overestimation of transmittance. In reality, however, optical window materials inherently absorb a portion of the incident light, particularly within specific spectral bands. The discrepancy between the simulated and experimentally measured transmittance therefore corresponds precisely to the absorptance of the material. Recognizing this, a calibration layer was introduced into the prediction model to account for this absorption effect. The calibration factors were derived directly from FTIR spectrometer measurements of a flat sapphire window, ensuring that the correction is physically meaningful rather than empirically fitted (Note S2, Supplementary information). By embedding this material-specific absorption information, the calibrated model accurately reflects true optical behavior, reducing prediction errors from over 8% to below 0.1% in the intrinsic absorption band (Fig. 2(j, k)). This physics-informed calibration not only enhances prediction accuracy but also provides a reliable foundation for subsequent inverse design and process optimization. Finally, leveraging the calibrated model, an interactive software for predicting the transmittance spectrum of anti-reflective sapphire windows was developed using MATLAB's App Designer. This software integrates the calibrated RPN and DPN models, allowing users to either input desired structural parameters to obtain the predicted transmittance spectrum or input a target spectral curve to receive recommendations for laser processing parameters. Thereby, this software is intended for real-time performance parameter feedback during the femtosecond laser fabrication of anti-reflective microholes, enabling the rapid construction of laser parameter-to-transmittance spectrum mapping.

2.2 Rapid iteration of femtosecond laser fabrication process

Following the successful construction and calibration of the bidirectional prediction model, this study employed it as a core intelligent agent to guide the rapid iterative optimization of the femtosecond laser fabrication process, aiming for the fast preparation of high-performance anti-reflective windows. As illustrated in Fig. 3(a), the fabrication utilized a high-repetition-rate (10 kHz) femtosecond laser burst-pulse combined with a rapid scanning strategy to achieve large-area, periodic microhole array fabrication. The structural parameters of the ARMs produced this way, however, are influenced by multiple laser processing parameters. These include laser energy, sub-pulse number, focusing position, and scanning speed (Fig. S6–S8, Supplementary information). Here, the calibrated prediction model was embedded into the process development cycle. This integration enabled a virtual assessment that directly maps laser parameters to the final optical performance, thereby significantly accelerating the search for the optimal process parameters (Fig. 3(b)).

The influence of laser focus position on microhole morphology was systematically investigated. As shown in Fig. 3(c), when the focusing position was gradually moved from above the material surface inward, both the microhole diameter and depth exhibited a nonlinear trend, initially increasing and then decreasing[47,73]. This phenomenon originates from the spatial evolution of laser energy distribution near the focal point. The energy density reaches an optimum when the focus is at or slightly below the surface, enabling effective material modification/ablation while avoiding excessive lateral heat diffusion. Consequently, the microhole diameter peaked (1.40 ±0.06 μm) at a focus position of 7 μm, while the depth reached its maximum (0.58 ±0.01 μm) at 6 μm. Model predictions indicated that the process conditions yielding the deepest microholes also produced the optimal broadband anti-reflective performance, with a peak transmittance reaching 93% (Fig. 3(d) and Fig. S9(a), Supplementary information). This aligns with the physical principle that deeper structures provide a more effective graded refractive index matching over a wider wavelength range[4,9]. The effect of sub-pulse count within an MHz burst mode on microhole morphology was further explored. As illustrated in Fig. 3(e), increasing sub-pulse number from 1 to 4 significantly enhanced the hole depth from 0.39 ±0.03 μm to 0.73 ±0.05 μm while the aperture remained nearly constant (1.40 ±0.07 μm), resulting in a high aspect ratio structure approaching 1:2. This is attributed to efficient energy coupling and thermal accumulation between multiple pulses[74–76]. Subsequent sub-pulses are more readily absorbed in regions pre-modified by earlier pulses, promoting continued material removal in the longitudinal direction[77–79]. Model-predicted spectra quantitatively revealed the improved anti-reflective performance resulting from this morphological optimization (Fig. 3(f)). At a wavelength of 4 μm, the transmittance increased from 90.9% to 94.4% with the pulse count (Fig. S9(b), Supplementary information).

Moreover, with the optimal focus position and sub-pulse count determined, a fine scan of laser energy was performed. As shown in Fig. 3(g), both microhole diameter and depth increased monotonically with laser energy, confirming its direct role in controlling ablation dimensions[80,81]. Corresponding model predictions showed the peak transmittance successfully rising from 91% to over 95% with increasing energy (Fig. 3(h)). Specifically, the transmittance at 4 μm began to plateau when laser energy reached 21 mW. A further increase to 25 mW still yielded significant improvement at 5 μm (Fig. S9(c), Supplementary information), consistent with the physical rule that longer wavelengths require greater microhole depth for effective anti-reflection. Additionally, microholes with periods of 1.6 μm, 1.8 μm, and 2.0 μm were fabricated by adjusting the scanning speed. Prediction results indicated that while a smaller period could broaden the anti-reflection bandwidth, it reduced the peak transmittance (Fig. S10, Supplementary information). For comparison, the uncalibrated model was also used to predict outcomes across these laser parameters. Although it captured the general trend, it failed to provide accurate feedback on the true transmittance spectra (Fig. S11, Supplementary information). In summary, this series of targeted, rapid process iterations fully validated the proposed machine-learning-assisted framework's capability to decipher the complex relationships between process, structure,

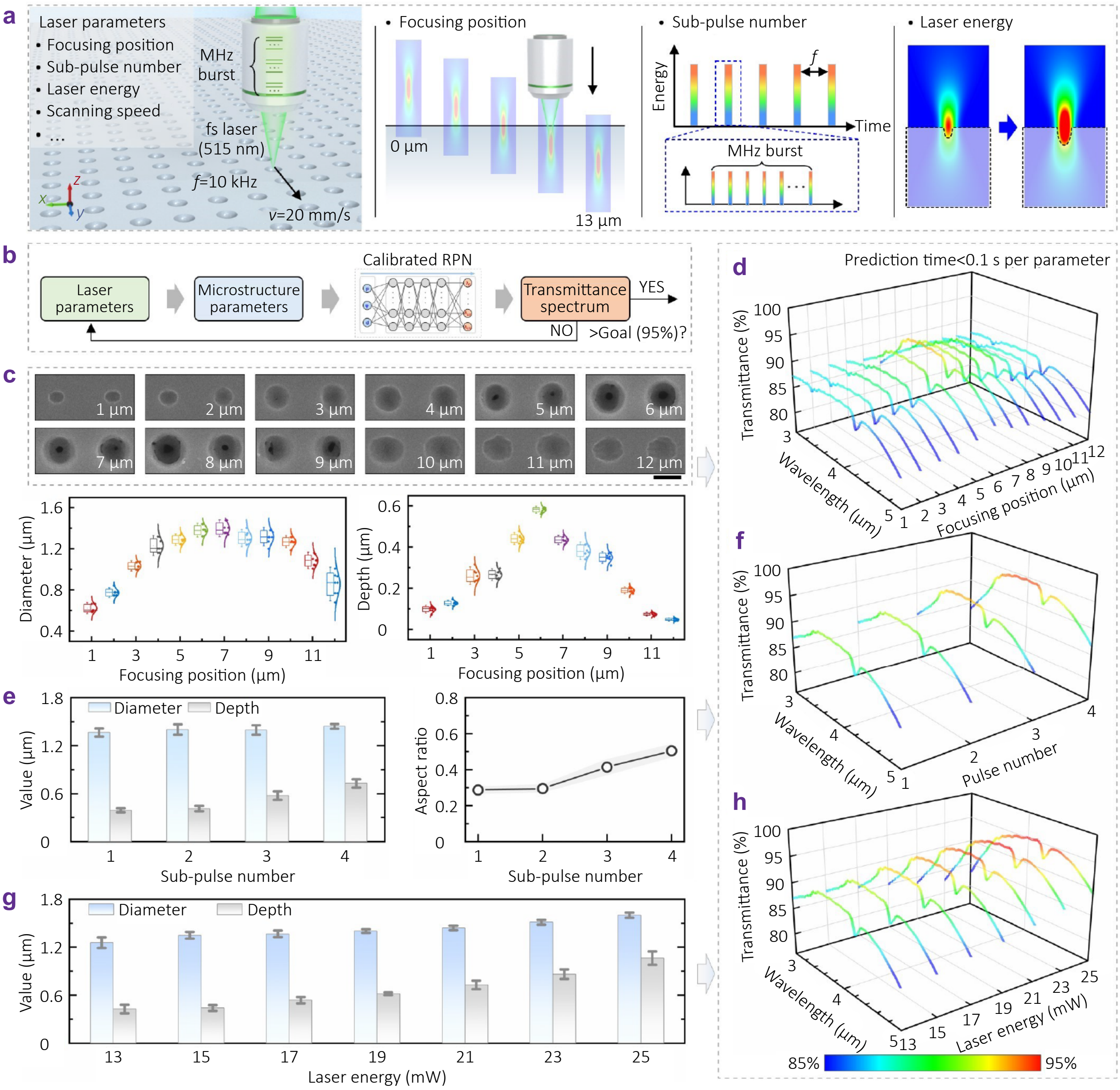

Fig. 3 | Application of ML model in laser processing iteration. (a) Schematic of the key parameters in femtosecond laser fabrication of anti-reflective micro-holes. (b) Schematic of the machine-learning-assisted rapid iteration process for femtosecond laser fabrication. (c) Effect of focus position on anti-reflective microhole morphology (Scale bar: 1 μm). (d) Calibrated RPN-predicted transmittance spectra of anti-reflection windows fabricated with different laser focus positions. (e) Influence of sub-pulse count on anti-reflective microhole formation. (f) Calibrated RPN-predicted transmittance of anti-reflection windows processed with varying numbers of sub-pulses. (g) Effect of laser energy on anti-reflective microhole characteristics. (h) Calibrated RPN-predicted transmittance of anti-reflection windows fabricated using different laser energies.

and performance. It substantially shortened the optimization cycle for manufacturing high-performance ARMs, moving beyond the traditional paradigm of experience-dependent trial-and-error.

2.3 Comprehensive performance of anti-reflective window

Based on the optimized laser parameters (Table S2, Supplementary information), a large-area (300 mm^2) anti-reflective sapphire window was fabricated (Fig. 4(a)). Figure 4(b–d) present the morphology and profile of the fabricated anti-reflective microholes, demonstrating high uniformity. Their average diameter and depth were approximately 1.60 μm and 1.05 μm, respectively. The transmittance of the window under normal incidence was measured using a FTIR spectrometer. The results show that, compared to a flat sapphire substrate, the anti-reflective sapphire window achieves an average transmittance enhancement of about 7% across the 3.3–6.0 μm band, with a peak transmittance of

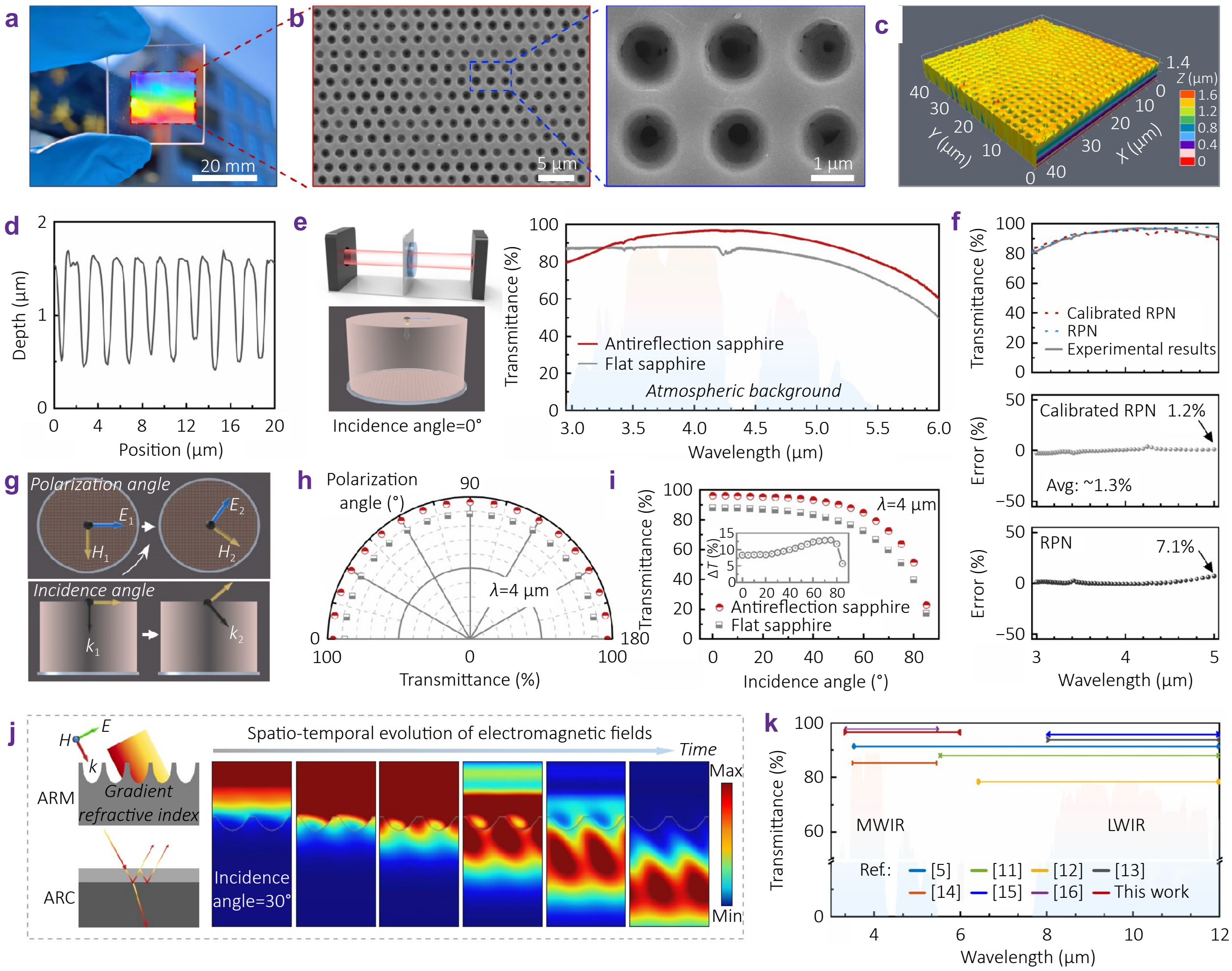

Fig. 4 | Analysis of optical properties of anti-reflective sapphire windows. (a) Macroscopic image of the anti-reflection sapphire window. (b, c) Scanning electron microscope (SEM) and laser scanning confocal microscope (LSCM) images of the ARM arrays. (d) Cross-sectional profile of the ARM arrays. (e) Experimentally measured transmittance spectra of the sapphire windows. (f) Comparison of transmittance spectrum predictions from the model before and after calibration. (g–i) Relationship between the transmittance of the anti-reflective sapphire and the polarization angle and incidence angle. (j) Comparison of the antireflection mechanisms between ARM and ARC, along with the simulated electromagnetic field transmission of ARM under oblique incidence. (k) Comparison of the optical transmittance performance of the sapphire antireflection window in this study with other works reported in the literature.

96.5% at the core MWIR wavelength of 4 μm (Fig. 4(e)). It should be noted that the measurements were conducted under non-vacuum conditions, which introduced fluctuations in the measurement curve around 4.3 μm due to the characteristic absorption of atmospheric CO_2. The transmittance spectrum predicted by the calibrated model closely matches the experimental results, showing a mean absolute error of only 1.3%. Compared to the pre-calibration model, its maximum error at the 5 μm wavelength was reduced from 7.1% to 1.2% (Fig. 4(f)). Furthermore, the influence of infrared light polarization angle and incidence angle on the transmittance performance of the anti-reflective sapphire window was investigated via simulation (Fig. 4(g)). Taking the 4 μm wavelength as an example, the transmittance remained stable as the polarization angle of the incident light varied from 0° to 180° (Fig. 4(h)). As the incidence angle increased from 0° to 70°, the transmittance enhancement of the anti-reflective sapphire relative to the substrate gradually became more pronounced (Fig. 4(i)). Even at a high incidence angle of 60°, the anti-reflective sapphire maintained a transmittance of approximately 85%. This advantage originates from the gradient refractive index antireflection mechanism of the ARMs. Under oblique incidence, regardless of how the incident angle changes, the gradient refractive index profile formed by the microstructures always exists, allowing the refraction/reflection of light at the interface to be gradually modulated by the continuously varying refractive index. Figure 4(j) and Fig. S12 (Supplementary information) show that under oblique incidence conditions, the ARMs still exhibit a localized electromagnetic field enhancement effect[49]. In contrast, courenventional ARCs rely on the optical path difference between different thin-film layers to achieve destructive interference of reflected light at each interface, thereby enhancing transmittance[10,82]. However, under oblique incidence, the propagation path of light within the thin films changes, causing the optical path difference to vary significantly with increasing incident angle. This disrupts the original destructive interference condition, leading to a rapid increase in reflection loss. These results demonstrate that the anti-reflective microholes impart the window with a wide-angle imaging capability, which is an advantage over conventional ARCs. Meanwhile, compared with other studies on ARMs, this work achieves good anti-reflective performance in the MWIR band (Fig. 4(k)).

Considering applications in solar cells, aircraft, and military equipment where windows are subjected to long-term sand impact and abrasion[10,19,83], the wear resistance of the anti-reflective sapphire was quantitatively studied using a sandpaper abrasion test (Fig. 5(a)). Given that sapphire has a high Mohs hardness of 9, SiC sandpaper (P220) with a Mohs hardness of 9.5 was selected. A 500 g weight was used as a load during sandpaper abrasion to maintain constant frictional force. Figure 5(b) presents LSCM images of the window surfaces after 50 abrasion cycles. Obvious scratches appeared on both the flat sapphire window and the anti-reflective sapphire window, while some anti-reflective microholes were worn down to a depth of approximately 0.4 μm. The appearance of scratches and the reduction in microhole depth led to a decrease in transmittance. Figure 5(c–f) show the transmittance spectra after different numbers of abrasion cycles. After 50 abrasion cycles, the

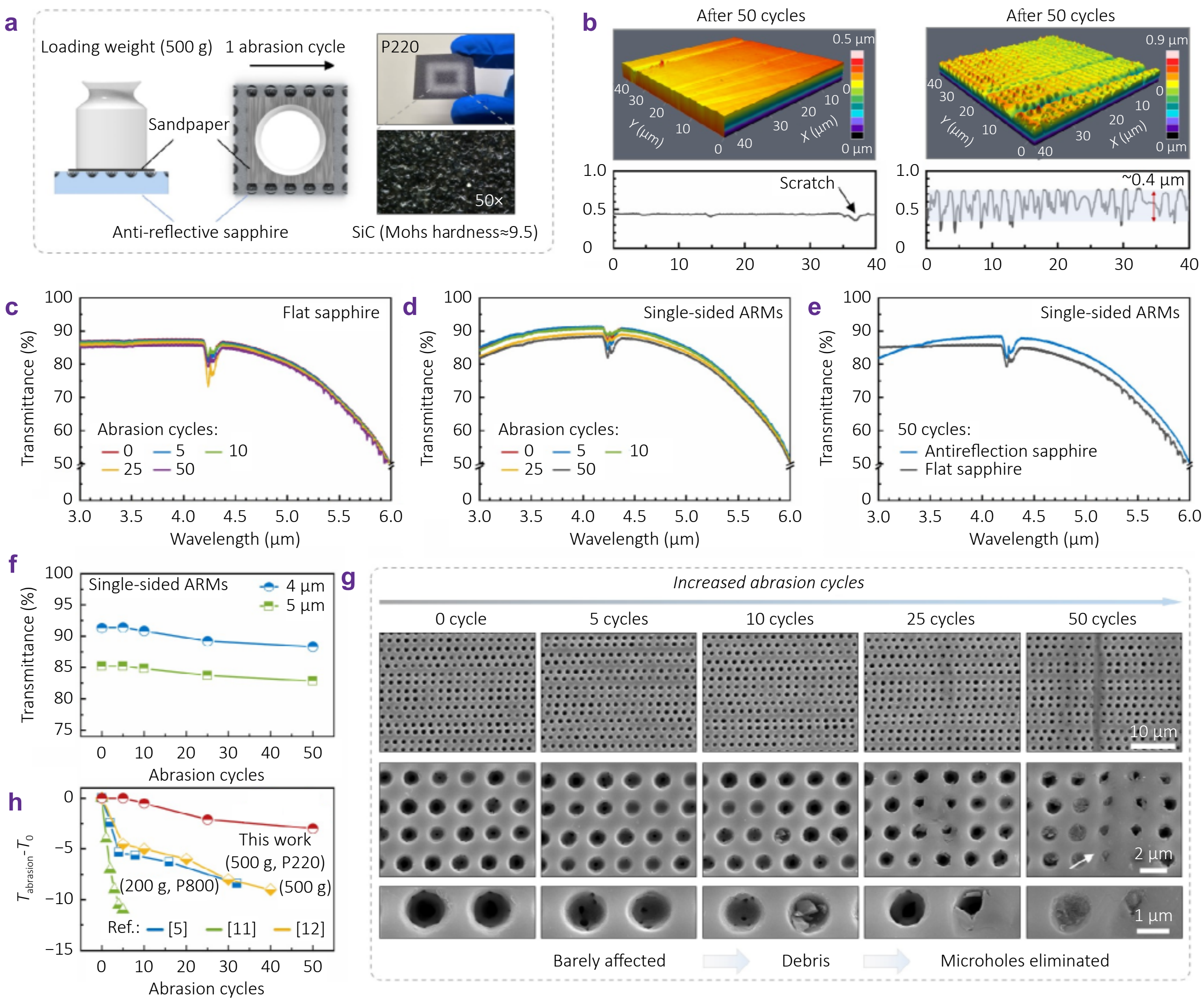

Fig. 5 | Analysis of mechanical properties of anti-reflective sapphire windows. (a) Schematic illustration of the sandpaper abrasion test, including the abrasion parameters and setup. (b) LSCM images of the flat sapphire and anti-reflective sapphire windows after sandpaper abrasion. (c–f) Transmittance spectra of the flat sapphire and anti-reflective sapphire windows after different numbers of abrasion cycles. (g) SEM images of the anti-reflective sapphire window surface after different numbers of abrasion cycles. (h) Comparison of the wear resistance of the anti-reflective sapphire window with other works reported in the literature.

transmittance of the two windows decreased by approximately 2% and 3%, respectively. It is worth noting that the transmittance of the anti-reflective sapphire remained almost unchanged during the first 10 abrasion cycles and only exhibited a noticeable decline between 10 and 50 cycles. This phenomenon can be explained by microscopic images of the worn microholes (Fig. 5(g)). From 0 to 5 abrasion cycles, the microholes showed almost no change. By 10 cycles, some debris appeared inside the microholes. With further abrasion, some microholes were gradually worn flat. The presence of debris causes light scattering, while the reduction in microhole depth diminishes the anti-reflection performance. Benefiting from the concave structural features and the inherent properties of sapphire, the fabricated ARMs exhibit less performance degradation under abrasion with heavier loads and higher-hardness sandpaper compared to other studies, indicating superior wear resistance (Fig. 5(h)). Additionally, the hydrophobicity of the anti-reflective sapphire was investigated (Fig. S13, Supplementary information). Compared to flat sapphire, the water contact angle on the anti-reflective sapphire increased by approximately 8°. After rinsing the window in water, no water droplets adhered, which is beneficial for subsequent cleaning and maintenance.

Infrared detection systems are often mounted on unmanned aerial vehicles for outdoor inspection and monitoring (Fig. 6(a)). The infrared window, a key component in such systems responsible for signal transmission and device protection, has a crucial impact on overall imaging performance. To evaluate the imaging performance of the anti-reflective sapphire window, it was mounted at the front of an infrared thermal camera to capture images. A humidifier was used to simulate rainy or foggy weather conditions, introducing interference into the thermal imaging process to mimic challenging outdoor inspection environments. Figure 6(b) presents infrared images captured with both a flat sapphire window and the anti-reflective sapphire window under normal and humidified (simulated rain/fog) conditions. The image contour features were effectively enhanced and extracted using Sobel edge detection combined with morphological dilation[84]. The results show that images captured through the anti-reflective sapphire exhibit more continuous and complete edge contours, along with richer detail. The overall image sharpness was quantified using the Brenner gradient, an indicator reflecting edge sharpness and contour definition[85]. Figure 6(c) shows that under non-interference conditions, the Brenner gradient value for images through the anti-reflective sapphire increased by approximately 9.2%. This performance advantage expanded further in the simulated rain/fog interference environment. For local contrast assessment, the standard mean difference was introduced to analyze texture representation (Fig. 6(d)). The anti-reflective sapphire yielded higher standard mean difference values than the flat sapphire under both normal and interference conditions, indicating greater local luminance variation and clearer texture information in its images[86]. Horizontal and vertical difference images further validated this conclusion from a spatial distribution perspective[87]. The anti-reflective sapphire provided a more uniform and stronger edge response in all directions (Fig. 6(e)). The Laplacian variance, a key parameter characterizing the intensity of high-frequency components in an image, is directly related to detail clarity[88]. The Laplacian variance for the anti-reflective sapphire was significantly higher than that for the standard window, a difference that became even more pronounced under interference conditions (Fig. 6(f, g)). This demonstrates that the ARM effectively enhances the transmission of high-frequency information, thereby maintaining superior detail reproduction under complex conditions. In summary, this comprehensive performance analysis of the anti-reflective window confirms that the microstructure endows the optical window with wide-angle capability, high transmittance, wear resistance, and superior imaging clarity. These combined attributes make it highly suitable for infrared thermal imaging applications in various extreme and complex environments.

3 Conclusions

In summary, this work presents a method for the rapid customization of high-performance anti-reflective windows using machine-learning-assisted femtosecond laser processing. The core innovation lies in integrating an experimentally calibrated bidirectional neural network with femtosecond laser machining technology, enabling rapid prediction and optimization linking laser parameters, structural parameters, and transmittance spectra. Specifically, to address simulation inaccuracies arising from intrinsic material absorption, a physical correction mechanism was introduced, which substantially enhanced the model's reliability. The trained model establishes a mapping relationship between laser parameters and anti-reflective performance, capable of predicting transmittance spectra within 0.1 s, a significant advantage over conventional simulations and experimental testing. Using a sapphire window as a demonstration case, the trained model guided the rapid optimization of the femtosecond laser process, efficiently identifying optimal laser parameter combinations for the target application. Test results confirm that the fabricated large-area (300 mm^2) anti-reflective sapphire exhibits broadband performance (3.3–6.0 μm) and high transmittance (~96.8% peak at 4.2 μm), alongside excellent wide-angle characteristics and good mechanical wear resistance. Furthermore, it demonstrates superior imaging clarity and more precise contour recognition capabilities. Looking ahead, this method can be extended to fabricate ARMs on different window materials according to specific application needs, thereby enhancing the service performance of infrared detection systems in extreme and complex environments.

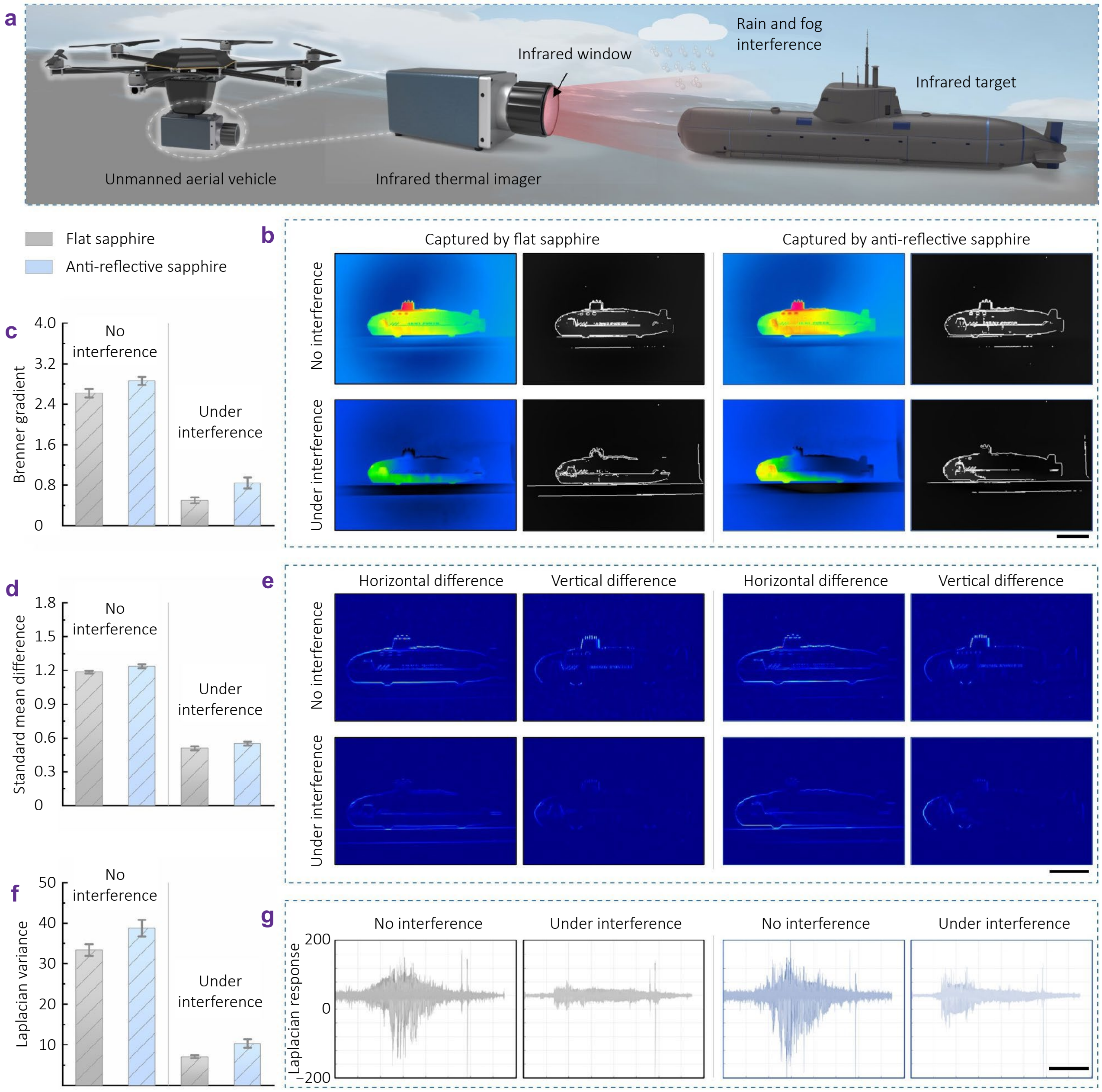

Fig. 6 | Analysis of infrared imaging performance for anti-reflective sapphire windows. (a) Schematic diagram of the infrared window assembled on an infrared thermal imager. (b) Infrared images captured under different imaging environments and their corresponding target contour recognition (Scale bar: 2 mm). (c) Comparison of Brenner gradient values for the captured infrared images. (d) Comparison of standard mean difference values for the captured infrared images. (e) Processed images after horizontal and vertical differentiation of the captured infrared images (Scale bar: 2 mm). (f) Comparison of Laplacian variance values for the captured infrared images. (g) Laplacian response of the captured infrared images (Scale bar: 2 mm).

4 Experiments and methods

4.1 ML model construction

The raw data used for model training was obtained through simulations conducted with the commercial software Ansys Lumerical FDTD Solutions (2022 R2). In the simulation model, the light source is set as a parallel beam, and the substrate material is configured as sapphire. Perfectly matched layer (PML) boundary conditions are applied in the direction of beam propagation, while periodic boundary conditions are set in the other two directions. Discrete fourier transform (DFT) monitor is used to acquire the transmittance spectrum. The ML model is built using a bidirectional multilayer perceptron architecture, achieving forward predictions from structural parameters to spectral responses and inverse designs from target spectra to structural parameters. The dataset contains three structural parameters as input vectors and fifty spectral response points as output vectors. During the data preprocessing stage, min-max normalization is applied to map the input and output data to the [0,1] range, enhancing the stability of model training. The dataset is randomly divided into training, validation, and testing sets in a ratio of 70%-15%-15%. The network architecture consists of two independent networks. An empirical trial-and-error approach combined with validation set performance was employed to determine the optimal network architecture (Note S3 and Fig. S14, Supplementary information). The forward network has a structure with four hidden layers, each containing 16 neurons, enabling nonlinear mapping from 3 dimensional inputs to 50 dimensional outputs. The backward network is similarly configured with four hidden layers, each with 16 neurons, achieving inverse predictions from fifty-dimensional spectral inputs to three-dimensional structural parameters. The hidden layers employ a sigmoid activation function to capture complex nonlinear relationships, and the output layer also uses a sigmoid activation function to ensure the output values remain within the normalized range. The training optimization strategy employs the Levenberg-Marquardt algorithm for network parameter optimization, which combines the advantages of gradient descent and the Gauss-Newton method, making it particularly suitable for training moderately sized datasets. The maximum training iterations for the forward network are set to 1000, while the backward network is set to 100, with a target error of 1×10^{-5}. An early stopping mechanism is introduced during training to monitor performance based on the validation set and prevent overfitting. Mean Square Error (MSE) is used as the primary loss function to guide parameter update directions. The performance evaluation system quantifies model prediction accuracy through R^2, while also conducting residual analysis and relative error assessment to ensure satisfactory accuracy in both forward prediction and inverse design tasks. All computations are implemented in MATLAB (R2023b), utilizing its neural network toolbox for model training and validation.

4.2 Fabrication

The experimental samples are sapphire windows that are polished on both sides, with dimensions of 30 mm × 30 mm × 1 mm. The samples are fixed on a three-axis motion platform (HS-DX3-V200, Hostech, China) using a custom fixture. The laser source used is a high-power ultrafast femtosecond laser (HR-300-1, Ultron Photonics, China) equipped with a pulse selection module. Detailed laser source parameters are available in Table S3 (Supplementary information). The beam is focused using a 40×, NA = 0.65 objective lens (GCO-213103, Daheng Optics, China). During process exploration, microhole arrays covering an area of 200 μm × 200 μm were fabricated under each set of laser parameters for morphology characterization. For optical performance testing, large-area microhole arrays with dimensions of 15 mm × 20 mm were fabricated for FTIR measurements. The samples after laser processing were etched with 20 wt% HF for 90 min, followed by ultrasonic cleaning in deionized water for 5 minutes.

4.3 Characterization

The morphology of the fabricated microholes is characterized using SEM (JSM-7900F, JEOL, Japan) and LSCM (LSM700, Carl Zeiss, Germany). The microhole structural parameters were obtained from SEM and LSCM images using ImageJ software. For each parameter set, ten randomly selected holes were measured, and the results are presented as the mean ±SD (Table S4, Supplementary information). The transmittance is evaluated using an FTIR spectrometer (Nicolet iS50, Thermo Fisher, USA). The transmittance was measured in transmission mode using a spectral resolution of 4 cm^{-1} over the 4000–400 cm^{-1} range. A total of 32 scans were averaged for each background and sample measurement to enhance the signal-to-noise ratio. With an incident beam diameter of ~10 mm, the transmittance spectrum was automatically calculated by the OMNIC software. The infrared imaging performance is tested using a mid-wave infrared thermal imager (ImageIR 8300, InfraTec GmbH, Germany). The calculation methods for image features are detailed in Note S4 (Supplementary information). During the calculation process, four parallel experimental images were analyzed, and the results are presented as the mean ±SD (Table S5, Supplementary information).

References

1. Sun TL, Qing GY, Su BL et al. Functional biointerface materials inspired from nature. *Chem Soc Rev* **40**, 2909–2921 (2011).
2. Wang YH, Zheng GX, Jiang N et al. Nature-inspired micropatterns. *Nat Rev Methods Primers* **3**, 68 (2023).
3. Bian J, Ma YX, Ling H et al. Scalable manufacturing of multifunctional insect wing membrane via interfacial lase-and-peel strategy. *Sci Adv* **11**, eaea6934 (2025).
4. Tadepalli S, Slocik JM, Gupta MK et al. Bio-optics and bio-inspired optical materials. *Chem Rev* **117**, 12705–12763 (2017).
5. Ding YL, Wang C, Jia XS et al. Laser-optical-field-modulation fabricating large-aperture dual-band antireflection windows for MWIR and LWIR imaging. *Int J Extrem Manuf* **8**, 025004 (2026).
6. Liu MJ, Wang ST, Jiang L. Nature-inspired superwettability systems. *Nat Rev Mater* **2**, 17036 (2017).
7. Zhang CJ, Liu BT, Yu SY et al. Long-lasting and stable anti-fog coating combined with active and passive strategy. *Nat Commun* **16**, 9003 (2025).
8. Jing XF, Ma JY, Liu SJ et al. Analysis and design of transmittance for an antireflective surface microstructure. *Opt Express* **17**, 16119–16134 (2009).
9. Bushunov AA, Tarabrin MK, Lazarev VA. Review of surface modification technologies for mid-infrared antireflection microstructures fabrication. *Laser Photonics Rev* **15**, 2000202 (2021).
10. Sarieddine R, Kadiri H, Guelorget B et al. A review on potential mechanically resistant materials for optical multifunctional surfaces: bioinspired surfaces with advanced properties. *Adv Mater Interfaces* **11**, 2300793 (2024).

11. Wang HR, Zhang F, Duan JA. Bioinspired broadband and mechanically-durable infrared antireflective subwavelength array by temporal-spatial shaping femtosecond laser micromachining. *Chem Eng J* **506**, 159928 (2025).
12. Zhang F, Duan JA, Zhou XF et al. Broadband and wide-angle antireflective subwavelength microstructures on zinc sulfide fabricated by femtosecond laser parallel multi-beam. *Opt Express* **26**, 34016–34030 (2018).
13. Cao H, Li YF, Wang G et al. Laser cleaning-assisted femtosecond laser direct writing of diamond antireflective microstructures with superhigh transmittance of 94.5% at 10.6 μm. *Small Structures* **6**, 2400590 (2025).
14. Zheng JX, Liu XQ, Tian KS et al. Nanofabrication of lithium niobate anti-reflective subwavelength structures for high power mid-infrared lasers. *Laser Photonics Rev* **18**, 2400546 (2024).
15. Yun B, Chen ZH, Wu ZL et al. Foci-multiplexed optical printing of high-transmittance infrared subwavelength-structured surface. *Opt Express* **33**, 8738–8748 (2025).
16. Liu XQ, Zhang YL, Li QK et al. Biomimetic sapphire windows enabled by inside-out femtosecond laser deep-scribing. *PhotoniX* **3**, 1 (2022).
17. Clapham PB, Hutley MC. Reduction of lens reflexion by the "Moth Eye" principle. *Nature* **244**, 281–282 (1973).
18. Teslenko A, Konstantinova T, Bushunov A et al. Antireflection microstructures on ZnSe for mid- and far-IR fabricated by femtosecond laser ablation assisted with wet chemical etching. *Sci Rep* **14**, 10743 (2024).
19. Chien KC, Kepenekci M, Tunell A et al. Scratch-resistant sapphire nanostructures with anti-glare, anti-fogging, and anti-dust properties. *Mater Horiz* **12**, 1796–1807 (2025).
20. Ding YL, Liu LP, Wang C et al. Bioinspired near-full transmittance MgF_2 window for infrared detection in extremely complex environments. *ACS Appl Mater Interfaces* **15**, 30985–30997 (2023).
21. Zhu CX, Ekinci H, Pan AX et al. Electron beam lithography on non-planar and irregular surfaces. *Microsyst Nanoeng* **10**, 52 (2024).
22. Tian XL, Li F, Tang ZY et al. Crosslinking-induced patterning of MOFs by direct photo- and electron-beam lithography. *Nat Commun* **15**, 2920 (2024).
23. Li SX, Huang GY, Xia H et al. Nanoimprint crystalithography for organic semiconductors. *Nat Commun* **16**, 3636 (2025).
24. Zhang F, Xu HC, Yang Q et al. Femtosecond laser microfabrication of artificial compound eyes. *Photonics* **11**, 264 (2024).
25. Liu RJ, Zhang DS, Li ZG. Femtosecond laser subtractive/additive-integrated biomimetic manufacturing for visible/infrared encryption and stimuli-responsive infrared decryption. *Int J Extrem Manuf* **7**, 045009 (2025).
26. Liao JN, Li ZG, Zhang DS. Bionic femtosecond laser manufacturing for impressionistic camouflage infrared display. *Int J Extrem Manuf* **8**, 015010 (2026).
27. Wu MN, Jiang L, Li TY et al. Efficient fabrication of infrared antireflective microstructures on a curved diamond-ZnS composite surface by using femtosecond bessel-like beams. *Opt Express* **31**, 28670–28682 (2023).
28. Yue Z, He LB, Cui QN et al. Fabrication of sapphire optical windows with infrared transmittance enhancement and visible transmittance reduction by femtosecond laser direct writing. *Opt Laser Technol* **188**, 112989 (2025).
29. Yang JJ, Zhou SK, Yang MT et al. Antireflection microstructures on a ZnS surface fabricated by femtosecond laser direct writing assisted with wet etching. *Opt Mater* **159**, 116597 (2025).
30. Li X, Shan C, Chen K et al. Bioinspired ZnS infrared detection window with enhanced broadband transmittance via green picosecond laser assisted with chemical etching. *ACS Appl Opt Mater* **3**, 1618–1627 (2025).
31. Ding YL, Wang C, Jia XS et al. Machine learning-driven optimization of burst femtosecond laser processing for high-performance anti-reflective windows. *ACS Appl Mater Interfaces* **17**, 65300–65309 (2025).
32. Fu JC, Jiang MT, Wang Z et al. Supercritical metalens at h-line for high-resolution direct laser writing. *Opto-Electron Sci* **3**, 230035 (2024).
33. Gao L, Zhang QM, Gu M. Femtosecond laser micro/nano processing: from fundamental to applications. *Int J Extrem Manuf* **7**, 022010 (2025).
34. Zhang JL, Ren FZ, Yang Q et al. Glass catfish inspired subaquatic abrasion-resistant anti-fouling window fabricated by femtosecond laser electrodeposition. *Int J Extrem Manuf* **7**, 015004 (2025).
35. Qiu P, Li J, Yuan DD et al. Adaptive beam-shaping enabled high-precision patterned laser micro-grooving. *Int J Extrem Manuf* **7**, 065002 (2025).
36. Li W, Xu L, Fu YZ et al. Femtosecond laser welding of non-optical-contact ceramic and fused silica. *Opt Lett* **51**, 532–535 (2026).
37. Tan YX, Mou ZC, Xu J et al. Femtosecond laser three-dimensional isotropic inscription in glass enabled by high-speed rotating slit beam shaping. *Int J Extrem Manuf* **8**, 015001 (2026).
38. Jia XS, Chen YY, Yi ZX et al. Tailoring sapphire-invar welds using burst femtosecond laser. *Light Adv Manuf* **7**, 3 (2026).
39. Li QY, Zhou F, Huang M. Femtosecond laser-induced sub-50-nm period nanogratings with ultrahigh uniformity on graphite under water immersion. *Int J Extrem Manuf* **8**, 015007 (2026).
40. Guo C, Li K, Liu ZL et al. CW laser damage of ceramics induced by air filament. *Opto-Electron Adv* **8**, 240296 (2025).
41. Xu K, Zheng MD, Huang LY et al. All-glass nanohole metalens by non-diffracting laser lithography. *Laser Photonics Rev* **19**, 2402006 (2025).
42. Zhang YM, Koike T, Yoshizaki R et al. Ultrahigh-speed laser drilling of transparent materials via transient electronic excitation. *Sci Adv* **11**, eadv4436 (2025).
43. Li Z, Xu JY, Chen YY et al. Filament-assisted combined pulse laser ablation of metal targets: mechanistic insights, efficiency enhancement, and spatial tolerance. *J Manuf Process* **160**, 371–388 (2026).
44. Ding YL, Wang C, Jia XS et al. Biomimetic ZnS windows fabricated by femtosecond laser optical field modulation assisted with wet etching for high-performance infrared monitoring of EV charging. *ACS Appl Mater Interfaces* **17**, 42462–42473 (2025).
45. Zhang SY, Fan MH, Niu PP et al. Modulating the periodicity of plasmonic lithography by high-repetition-rate laser-driven heat accumulation. *Opt Lett* **50**, 5242–5245 (2025).
46. Jiang L, Wang AD, Li B et al. Electrons dynamics control by shaping femtosecond laser pulses in micro/nanofabrication: modeling, method, measurement and application. *Light Sci Appl* **7**, 17134 (2018).
47. Han WN, Zhao KL, Wei DH et al. Femtosecond laser non-diffracting-beam lithography via phase modulation for dielectric metasurface fabrication. *Adv Mater* **38**, e21635 (2026).
48. Han RZ, Zhang YC, Jiang QL et al. Ultrafast dynamics of femtosecond laser-induced high spatial frequency periodic structures on silicon surfaces. *Opto-Electron Sci* **3**, 230013 (2024).
49. Münzer HJ, Mosbacher M, Bertsch M et al. Local field enhancement effects for nanostructuring of surfaces. *J Microsc* **202**, 129–135 (2001).
50. Marathay AS, McCalmont JF. Vector diffraction theory for electromagnetic waves. *J Opt Soc Am A* **18**, 2585–2593 (2001).
51. Song YM, Choi HJ, Yu JS et al. Design of highly transparent glasses with broadband antireflective subwavelength structures. *Opt Express* **18**, 13063–13071 (2010).
52. Chen LW, Zhang CJ, Zhou AH et al. Surface adhesion engineering for armored metasurfaces and beyond. *Adv Sci* **13**, e14000 (2025)

53. Gao Z, Wang C, Jia XS et al. Ultrahigh transmittance biomimetic fused quartz windows enabled by frequency-doubling femtosecond laser processing. *ACS Appl Mater Interfaces* **17**, 43944–43956 (2025).
54. Wang HR, Li BW, Hu LB et al. Manufacturing anti-reflective subwavelength structures on ZnS using femtosecond laser Bessel beam with burst mode. *Biomimetics* **9**, 655 (2024).
55. Yuan H, Zhong ZQ, Zhang B. Neural network assisted end-to-end design for broadband high diffraction efficiency full-color meta-holograms. *Laser Photonics Rev* **19**, e00946 (2025).
56. Chi HB, Hu YQ, Ou XN et al. Neural network-assisted end-to-end design for full light field control of meta-optics. *Adv Mater* **37**, 2419621 (2025).
57. Zhao MZ, Wei HL, Mao YM et al. Predictions of additive manufacturing process parameters and molten pool dimensions with a physics-informed deep learning model. *Engineering* **23**, 181–195 (2023).
58. Karniadakis GE, Kevrekidis IG, Lu L et al. Physics-informed machine learning. *Nat Rev Phys* **3**, 422–440 (2021).
59. Zhang RY, Strickland J, Yang F et al. Rapid residual stress simulation and distortion mitigation in laser additive manufacturing through machine learning. *Addit Manuf* **102**, 104721 (2025).
60. Zhang XN, Zhou L, Feng GD et al. Laser technologies in manufacturing functional materials and applications of machine learning-assisted design and fabrication. *Adv Compos Hybrid Mater* **8**, 76 (2025).
61. Saifullah Y, Wu NX, Wang HP et al. Deep learning in metasurfaces: from automated design to adaptive metadevices. *Adv Photonics* **7**, 034005 (2025).
62. Barati Sedeh H, George RC, Lai FX et al. Toward the meta-atom library: experimental validation of machine learning-based mie-tronics. *Adv Photonics* **7**, 034005 (2025).
63. Somerville LD, Leslie P, Jordan S et al. Comparing reflected and emitted radiometric signal levels in short-wave infrared, extended short-wave infrared, mid-wave infrared, and superband (short-wave infrared through mid-wave infrared) optical systems. *Opt Eng* **64**, 023102 (2025).
64. Huang LC, Han ZY, Wirth-Singh A et al. Broadband thermal imaging using meta-optics. *Nat Commun* **15**, 1662 (2024).
65. Gu ZF, Gao YX, Zhou KS et al. Surface-patterned chalcogenide glasses with high-aspect-ratio microstructures for long-wave infrared metalenses. *Opto-Electron Sci* **3**, 240017 (2024).
66. Zhang SF, Gao LN, Zhao YD et al. Integrated metasurface-freeform system enabled multi-focal planes augmented reality display. *Opto-Electron Sci* **5**, 250031 (2026).
67. Mu G, Tan YM, Bi C et al. Visible to mid-wave infrared PbS/HgTe colloidal quantum dot imagers. *Nat Photonics* **18**, 1147–1154 (2024).
68. Thomas ME, Andersson SK, Sova RM et al. Frequency and temperature dependence of the refractive index of sapphire. *Infrared Phys Technol* **39**, 235–249 (1998).
69. Chen YA, Chien KC, Chen IT et al. Sapphire nanophotonics: fabrication challenges and optical properties. *Micro Nano Eng* **14**, 100115 (2022).
70. Massel SR. Extended refraction-diffraction equation for surface waves. *Coastal Eng* **19**, 97–126 (1993).
71. Choy TC. *Effective Medium Theory: Principles and Applications* 2nd ed (Oxford University Press, Oxford, 2015).
72. Smith BC. *Fundamentals of Fourier Transform Infrared Spectroscopy* (CRC Press, Boca Raton, 2011).
73. Jiang X, Xu XJ, Zhou HB et al. Femtosecond laser burst mode combined with wet etching for fabricating surface microholes on sapphire. *Appl Phys A* **131**, 888 (2025).
74. Wang AD, Sopeña P, Grojo D. Burst mode enabled ultrafast laser inscription inside gallium arsenide. *Int J Extrem Manuf* **4**, 045001 (2022).
75. Fraggelakis F, Lingos P, Tsibidis GD et al. Double-pulse femtosecond laser fabrication of highly ordered periodic structures on au thin films enabling low-cost plasmonic applications. *ACS Nano* **19**, 23258–23275 (2025).
76. Yin JB, Lin ZY, Ji LF et al. Femtosecond laser micro/nano-processing via multiple pulses incubation. *Opto-Electron Technol* **1**, 250003 (2025).
77. Shi LP, Yan J, Zhang SY et al. Burst laser-driven plasmonic photochemical nanolithography of silicon with active structural modulation. *Ultrafast Sci* **5**, 0084 (2025).
78. Xu LR, Tao JC, Li ZG et al. Femtosecond laser ultrafast photothermal exsolution. *Int J Extrem Manuf* **6**, 055002 (2024).
79. Obata K, Kawabata S, Hanada Y et al. High performance micromachining of sapphire by laser induced plasma assisted ablation (LIPAA) using GHz burst mode femtosecond pulses. *Opto-Electron Sci* **3**, 230053 (2024).
80. Li MJ, Chen WB, Deng CS et al. Recent advances in femtosecond direct laser writing of micro-optical imaging components. *Int J Extrem Manuf* **8**, 022011 (2026).
81. Mauclair C, Najih B, Comte V et al. Dynamic spatial beam shaping for ultrafast laser processing: a review. *Opto-Electron Sci* **4**, 250002 (2025).
82. Raut HK, Ganesh VA, Nair AS et al. Anti-reflective coatings: a critical, in-depth review. *Energy Environ Sci* **4**, 3779–3804 (2011).
83. Papadopoulos A, Skoulas E, Mimidis A et al. Biomimetic omnidirectional antireflective glass via direct ultrafast laser nanostructuring. *Adv Mater* **31**, 1901123 (2019).
84. Kittler J. On the accuracy of the Sobel edge detector. *Image Vision Comput* **1**, 37–42 (1983).
85. Chen LL, Han M, Wan HL. The fast iris image clarity evaluation based on brenner. In *2013 2nd International Symposium on Instrumentation and Measurement, Sensor Network and Automation (IMSNA)* 300–302 (IEEE, 2013). http://doi.org/10.1109/IMSNA.2013.6743274.
86. Yin WM, Liu WS. Improved SMD image evaluation function based on pixel difference. In *International Conference on Computer Intelligent Systems and Network Remote Control (CISNRC)* (2020). http://doi.org/10.12783/dtcse/cisnr2020/35165.
87. Choi C, Yoon Y, Lee J et al. Simultaneous recognition of horizontal and vertical text in natural images. In *14th Asian Conference on Computer Vision* 202–212 (Springer, 2019). https://doi.org/10.1007/978-3-030-21074-8_16.
88. Wan XQ, Liu H, Chen F et al. LFAH-Net: laplacian frequency aware hierarchical network for hyperspectral image classification. *Digit Signal Process* **168**, 105561 (2026).

Acknowledgements

We are grateful for financial supports from National Key R&D Program of China (Grant No. 2023YFB4605500), Key Program for Basic Research (Grant No. JCKY2024210A001), National Natural Science Foundation of China (Grant No. 52105498), Natural Science Foundation of Hunan Province (Grant No. 2023JJ40736, Grant No. 2026JJ50177), State Key Laboratory of Ultrafast Optical Science and Technology (Grant No. 2025SKL-uFAST-KF22), and State Key Laboratory of Precision Manufacturing for Extreme Service Performance (Grant No. ZZYJKT2023-08).

Author contributions

C. Wang, X. Jia, and J. Duan proposed the original idea and supervised the project; Y. Ding and X. Jiang constructed the model and performed the experiment; L. Liu, W. Han, D. Yan and N. Lin helped perform the analysis; Z. Gao and S. Wang helped perform the experiment and data analyses.

Competing interests

The authors declare no competing financial interests.

Supplementary information

Supplementary information for this paper is available at https://doi.org/10.29026/oes.2026.260004

Published by Editorial Office of *Opto-Electronic Science*, Institute of Optics and Electronics, Chinese Academy of Sciences.